ACES Asian Chemical Editorial Society

doi.org/10.1002/asia.202300343

CHEMISTRY AN ASIAN JOURNAL Research Article

www.chemasianj.org

Phase-Controlled Pd-Sn Nanostructures via Co-Digestive Ripening: Catalytic Performance for Base-Free Oxidation of Benzyl Alcohol

Geetanjali Bhatia and Balaji R. Jagirdar*[a]

Abstract: Diluting the precious metal to be used for catalysis with an abundant and non-precious metal to form alloy/intermetallic nanostructures is of great interest owing to the cost-effectiveness of the catalyst. The physicochemical properties of such bimetallic nanostructures are influenced by the atomic ordering of different atoms in the system, generally enhancing the catalytic activity, selectivity, and durability compared to their monometallic counterparts. To understand the relationship between the structure and the activity of the catalyst, phase-controlled synthesis of alloy/intermetallic nanostructures is crucial. Easy and scalable synthesis of such nanostructures with phase control presents a true challenge. We exploited a colloidal-based synthetic route termed 'co-digestive ripening' to prepare Pd–Sn alloy/intermetallic nanostructures. Oleylamine capped Pd and Sn colloids were utilized to obtain network-like Pd_3Sn and grape-like Pd_2Sn nanostructures. Temperature and the stoichiometric ratio between Pd and Sn played significant roles in achieving phase control. The mixture of ligands (oleylamine and trioctylphosphine) in the synthetic procedure resulted in the formation of well-separated nanoparticles (2.9 ± 0.5 nm) in the case of Pd_3Sn and few nm-sized particles along with aggregates in the case of Pd_2Sn. Pd–Sn nanostructures showed enhanced activity and selectivity as compared to their monometallic counterparts for the catalytic performance towards oxidation of benzyl alcohol.

Introduction

Noble metal nanostructures (NMNSs) are ubiquitous in modern chemistry due to their potential applications in several technological fields, such as electrochemistry, electronics, magnetic storage, sensing, and catalysis.[1–4] The outstanding catalytic activities of NMNSs, especially of palladium (Pd)-based systems, in various chemical and electrochemical reactions, such as hydrogenation, oxidation, and coupling reactions, have gained much attention.[5] However, due to the limited reserves of noble metals, it has become imperative to be less dependent on the NMNSs. In this direction, mixing the precious metal with a non-precious metal to produce intermetallic compounds and alloys has proven to be an effective method for better use of the precious metal.[6–8] The incorporation of a second metal as an alloy/intermetallic structure, controls the surface composition of the catalyst by modifying the electronic properties and the geometry of the adsorption sites of the material.[9,10] Another exciting feature of such bimetallic nanostructures is the arrangement of atoms, i.e., disordered for alloy and ordered for intermetallic, which dramatically alters the properties of nanostructures, even when they have identical compositions.[11] Armbrüster et al. documented the influence of the ordering of atoms on the selectivity of acetylene semi-hydrogenation using a PdCu catalyst.[12] Despite having similar compositions, the ordered intermetallic phase of PdCu with that of the CsCl structure, it showed higher ethylene selectivity than the disordered alloy of PdCu bimetallic with fcc phase. This was ascribed to a great extent of site isolation due to the large Pd–Pd distance in the intermetallic structure compared to that in an alloy. Bimetallic nanostructures consisting of noble metals and inexpensive transition metals, which reduce the noble metal usage, and the overall cost of the catalyst are particularly intriguing.

To obtain the bimetallic nanoalloys with the necessary structure and property combination, it is crucial to carefully select the synthetic methodology as it determines the final morphology and, in turn, the catalytic capabilities that these materials exhibit. In this regard, a straightforward synthetic route that could also provide some insights into the mechanism of formation of alloys and intermetallic nanostructures is essential. Amongst various preparation techniques, the colloidal synthetic route stands out in facilitating the synthesis of nanostructures from the initial combination of atoms into nanoclusters to their growth through surfactants or capping agents. This versatile approach imparts an incomparable and precise tuning over nanomaterials' properties allowing the production of a variety of nanomaterials with control over size, shape, composition, and phase in a simple and cost-effective manner.[13–15]

Pd–Sn systems find essential applications in the ethanol oxidation reaction,[13,16] water denitration,[17] selective oxidation of alcohols,[18] and selective hydrogenations of unsaturated aldehydes,[19,20] hexa- and butadienes[21,22] etc.[23] Herein we report, the colloidal-based route, known as 'co-digestive ripening,'[24] in combination with solvated metal atom dispersion (SMAD) approach to obtain the random alloy and intermetallic nanostructures of Pd–Sn with phase control. Numerous routes, such as the wet chemical method, chemical reduction method, and oil-bath method have been employed for their synthesis, however, scale-up, monodispersity of particle

[a] G. Bhatia, B. R. Jagirdar
Department of Inorganic and Physical Chemistry
Indian Institute of Science, Bangalore
Karnataka, 560012 (India)
E-mail: jagirdar@iisc.ac.in

Supporting information for this article is available on the WWW under https://doi.org/10.1002/asia.202300343

size, phase purity and reproducibility remain as challenges.[25–27] Co-digestive ripening is a unique approach that has been successfully employed to synthesize various alloy and intermetallic nanostructures earlier.[28–31] In this process, colloids of individual metal elements are mixed at room temperature, followed by refluxing in a suitable solvent in the presence of the digestive ripening agent or capping agent.[24] It involves the ligand-assisted interparticle atom transfer during reflux, facilitating the formation of bimetallic structures.[32] This method enables the synthesis of size, shape and phase controlled bimetallic nanoparticles at milder temperatures than those used in conventional techniques. Since the process of co-digestive ripening involves the transfer of atoms from one nanoparticle to another, it is thus possible to obtain bimetallic structures with different sizes and compositions by modulating the parameters such as the stoichiometric ratio of the starting colloids, reflux temperature, and digestive ripening agent, however, much more conveniently than other synthetic methodologies.[28–30] The colloids utilized for co-digestive ripening were prepared by the solvated metal atom dispersion (SMAD) approach, an effective way to prepare stable and homogeneous colloids of metal nanoparticles developed by Klabunde and co-workers.[33] No metal salt precursor or reducing agents are used in this process, which renders the approach facile and involves no tedious purification procedures. Additionally, the SMAD method offers the ability to prepare nanoparticles of highly reactive metals (Sn in this case) in their zero-oxidation state.[34] Reproducibility and scalability are the main advantages of the combination of the SMAD and co-digestive ripening, making it a reliable and efficient approach for synthesizing alloy and intermetallic nanostructures. This one-pot synthetic strategy, therefore, can produce a variety of nanoalloys/intermetallics at much larger scale and relatively milder conditions which is crucial to explore different applications of such materials.

Oxidation of benzyl alcohol to benzaldehyde is of great importance due to its comprehensive utilization in various industries such as pharmaceuticals, dyes, food, and agrochemicals.[35] Industrial scale benzyl alcohol oxidation involves the usage of expensive stoichiometric oxidants such as dichromate, chromic acid, and permanganate.[36] The production of large quantities of undesirable, often toxic, by-products is one of the major concerns in the conventional techniques. Aiming at the environmentally and economically friendly synthesis of benzaldehyde, the use of benign oxidants such as oxygen or air in the presence of a heterogeneous catalyst are highly desirable.[37] However, the aerobic oxidation of alcohols in the liquid phase generally employs the use of alkalis such as K_2CO_3 to accelerate the reaction;[38] use of such strong alkalis leads to corrosion and a large amount of basic waste. To circumvent these issues, a number of bimetallic catalysts have been reported in the literature, which are mainly based on precious metals such as Pd, Pt, Ag, and Au, with Pd–Au as the most widely studied system.[39–41] The need to achieve base-free selective oxidation of benzyl alcohol using a clean oxidant (O_2) and a cost-effective catalyst prompted us to explore the Pd–Sn nanostructures for catalysis. Phase-controlled Pd_2Sn and Pd_3Sn nanostructures were successfully realized by careful optimization of the synthetic conditions. Pd–Sn nanostructures were then tested for the selective oxidation of benzyl alcohol as a model reaction. The results of these studies have been discussed herein.

Results and Discussion

Pd And Sn Nanocolloids

THF-stabilized Pd nanoparticles were found to be quite unstable towards precipitation of particles compared to those of the Sn samples. The powder XRD patterns (Figures 1a, 1b) could be referenced to the fcc phase of Pd (JCPDS No. 46–1043) and the tetragonal phase of Sn (JCPDS No. 04-0673), respectively. The BFTEM image (Figure 1c) of the Pd-THF colloidal nanoparticles revealed small-sized, irregularly shaped nanoparticles that are largely aggregated. Fringes in the high-resolution (HRTEM) image (Figure 1d) with a d-spacing value of 2.24 Å correspond to the (111) plane of Pd(0). The selected area electron diffraction (SAED) pattern (Figure 1e) exhibited rings that could be indexed to the characteristic planes of fcc Pd and confirms the crystalline nature of Pd nanoparticles. The BFTEM image (Figure 1f) corresponding to the Sn-THF colloid shows the presence of nearly spherical polydispersed nanoparticles. A shell formation on a few Sn nanoparticles was evidenced in the BFTEM images owing to the formation of tin oxides on their surface. This is due to the unavoidable exposure of nanoparticles to air while sampling. No peaks of tin oxides were, however noted in the PXRD pattern. The d-spacing value of 2.91 Å for the fringes in the HRTEM image (Figure 1g) could be indexed to the (200) plane of the tetragonal phase of Sn(0). The selected area electron diffraction pattern (Figure 1h) confirms

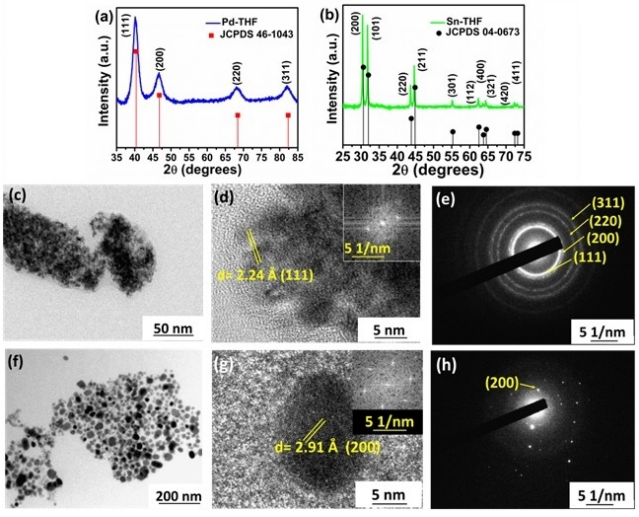

Figure 1. (a, b) PXRD patterns of Pd-THF and Sn-THF, respectively; (c) BFTEM image, (d) HRTEM image, and (e) SAED pattern of Pd-THF, respectively; (f) BFTEM image, (g) HRTEM image, and (h) SAED pattern of Sn-THF, respectively.

the tetragonal phase and the crystalline nature of Sn nanoparticles.

Oleylamine Stabilized Pd And Sn Colloids Via Room Temperature Digestive Ripening

The stability of the as prepared nanocolloids synthesized by the SMAD method towards precipitation of particles is determined by the extent of polydispersity and aggregation of nanoparticles. The nucleation and growth of nanoparticles in this methodology take place at the bottom of the reactor once the matrix of 'solvated metal atoms'[42] starts warming up to room temperature. The growth process, therefore, could be halted by introducing the capping agent at the beginning of the SMAD experiment. The capping agent stabilized colloids could be further refluxed at or near the boiling point of the solvent for the size-tuning of nanoparticles. The post-synthetic addition of a capping agent in the as-prepared colloids could also be done, followed by vigorous stirring, and refluxing to attain stability and monodispersity of colloids. This process is known as 'digestive ripening'.[43] Digestive ripening had even been achieved at room temperature, as reported by Jagirdar et al. in the case of Mg and Ca nanoparticles.[44,45] As the matrix warms up, the capping agent already in the SMAD reactor arrests the growth of metal clusters before the colloid attains room temperature forming stable colloids.[44] Room temperature ripening of Pd nanoparticles in the presence of dodecanethiol was even reported by Pileni and co-workers.[46] In the current work, room temperature digestive ripening of Pd and Sn nanoparticles was attempted by introducing oleylamine in the SMAD reactor under vigorous stirring for 2–2.5 h. Oleylamine has been widely used for synthesizing various metal-based nanostructures in a solution-based synthesis, where it acts as a surfactant, solvent, and/or reductant.[47] It effectively binds with the surface atoms of palladium and tin to produce stable colloidal suspensions of nanoparticles in organic solvents and also Pd–Sn bimetallic nanostructures.[13,17,25,27] In the case of oleylamine-stabilized Pd-THF (Pd-OLA-THF) colloid, the PXRD pattern (Figure 2a) was featureless while well-defined peaks were observed corresponding to Pd-THF sample (Figure 1a) without oleylamine. This indicates that there is a change in size and crystallinity of Pd-THF particles upon incorporation of OLA. In the case of Sn-OLA-THF colloid, PXRD peaks could be referenced to tetragonal Sn(0) (Figure 2b). BFTEM image shows irregular Pd nanostructures with multiple branches (Figure 2c). Amine-cappedPd(0) nanostructures with such morphologies have been reported in the literature.[46,48] In general, selective binding of the capping agent and the extent of its coverage on the surface of particles leads to the anisotropic growth of nanostructures.[49] Additionally, some reports attribute the formation of branched or worm-like structures to the diffusion-limited growth in the case of a weak interacting ligand with metal nanocrystals.[46] Fringes could be seen in a very few regions of the HRTEM image (Figure 2d) attributable to the (111) plane of the fcc phase of Pd(0). In the SAED pattern (Figure 2e), diffused rings were noted with faint spots on the

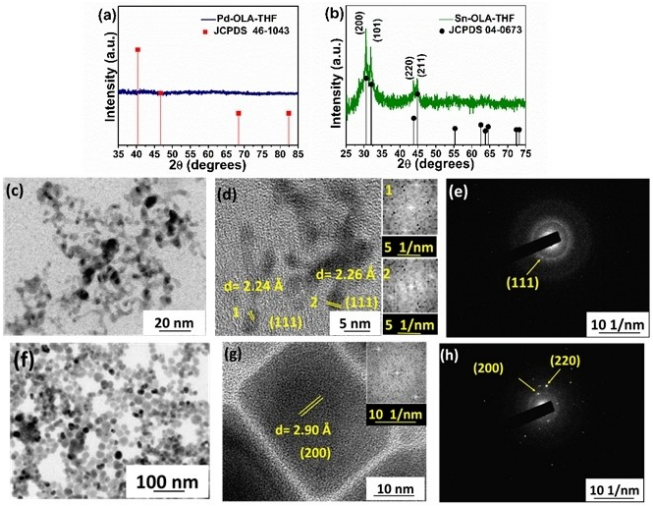

Figure 2. (a, b) PXRD patterns of Pd-OLA-THF and Sn-OLA-THF nanoparticles, respectively; (c) BFTEM image, (d) HRTEM image, and (e) SAED pattern of Pd-OLA-THF, respectively; (f) BFTEM image, (g) HRTEM image, and (h) SAED pattern of Sn-OLA-THF, respectively.

innermost ring that could be assigned to the (111) plane of *fcc* Pd(0). Weakly aggregated, monodispersed spherical Sn nanostructures with few multi-faceted particles could be observed in the BFTEM image (Figure 2f). Relatively strong binding of OLA with the surface atoms of Sn clusters could be responsible for breaking down and re-deposition of Sn clusters resulting in room-temperature ripening.[44] Even in this case, fringes were observed in a few regions of the HRTEM image (Figure 2g). The HRTEM and SAED data (Figure 2h) corroborate with the PXRD measurements. The formation of spherical nanoparticles that are nearly monodisperse in the case of oleylamine-capped Sn nanoparticles highlights the isotropic interaction of the Sn surface with OLA.

Synthesis Of Pd_3Sn and Pd_2Sn Nanostructures Via Co-digestive Ripening Of Pd and Sn

According to the phase diagram of bulk Pd–Sn system, several phases such as Pd_3Sn, Pd_2Sn, PdSn, $PdSn_2$, $PdSn_3$, Pd_3Sn_2, and $PdSn_4$ are known to exist.[50] Among the various phases, Pd_3Sn and Pd_2Sn have been explored for catalytic applications at the nanoscale.[13,17,25] Pd_3Sn exists in the $L1_2$ (ordered intermetallic) and the fcc phase (disordered alloy); Pd_2Sn is an intermetallic system with orthorhombic phase.[25,51] With the objective of diluting Pd with Sn to produce bimetallic nanostructures in a simple manner with phase control, we synthesized two different phases of the Pd–Sn system. Pd_3Sn is structurally identical to Pd (both fcc phases) and offers a more accurate comparison with the catalytic performance of monometallic Pd.[52] Pd_2Sn is an intermetallic compound which is expected to have better durability, selectivity, and catalytic activity than the random alloys as observed in the previous literature reports for ordered phases.[11,53] Therefore, we only focused on Pd_3Sn and Pd_2Sn phases to evaluate the effect of dilution of Pd by Sn on the

catalytic activity as a proof-of-concept. However, other phases could also be accessed by varying the reaction parameters during the co-digestive ripening process.

Pd_3Sn nanostructures were prepared by employing co-digestive ripening of Pd and Sn colloids obtained from the SMAD experiments. Co-digestive ripening was performed using Pd-OLA-THF and Sn-OLA-THF colloids in a ratio of 4:1 at a reflux temperature of 165 °C (mesitylene was used as a solvent) for 12 h. The ratio of metal to OLA was taken as 1:10. Peaks in the PXRD pattern (Figure 3a) were found to be shifted towards lower 2Θ values with respect to Pd(0), indicating the insertion of Sn atoms into the Pd lattice, as demonstrated previously.[54,55,56] In this case, the peak values at 2Θ = 39.31°, 45.04°, and 66.88° are very close to the values of the reference patterns for both ordered (ICDD 01–072-2873) and disordered (ICDD 03–066-0022) phases of the Pd_3Sn system and to the values reported in the literature for Pd_3Sn nanoparticles.[57,58] This confirms the formation of Pd_3Sn nanoparticles; however, it is difficult to differentiate between the ordered and the disordered phases using PXRD due to their nearly identical patterns. The only identity of the intermetallic Pd_3Sn that differentiates it from the fcc phase is the presence of the superlattice due to its highly ordered structure. However, in the reference PXRD pattern, the intensity of the superlattice peaks is 0.1% with respect to the most intense peak of Pd_3Sn, which is too weak to be observable. Pd_3Sn colloid was found to be stable towards precipitation of particles. For the TEM measurements, samples were prepared from the brown-colored supernatant part and the black precipitate. BFTEM images of the samples prepared using the Pd_3Sn-OLA precipitates revealed the presence of worm-like nanostructures forming networks (Figures 3b,3c). In the HRTEM image (Figure 3d), fringes with d-spacing values of 2.30/2.31 and 1.99 Å were noted, which could be indexed to the (111) and the (200) planes of fcc Pd_3Sn nanoparticles, respectively.[51] No spots from the corresponding FFT patterns (Figure 3d, 1–4), for the superlattice structure were observed, which indicates that Pd_3Sn is in the form of a disordered phase (fcc), i.e. random alloy. The d-spacing in the SAED pattern (Figure 3e), corroborates with the HRTEM data. Area mapping of the sample confirmed the homogeneous distribution of Pd and Sn (Figures 3f–3 h).Bulk elemental analysis was done using SEM-EDS, which revealed the ratio of Pd:Sn to be roughly 75:25 (Figure S1).

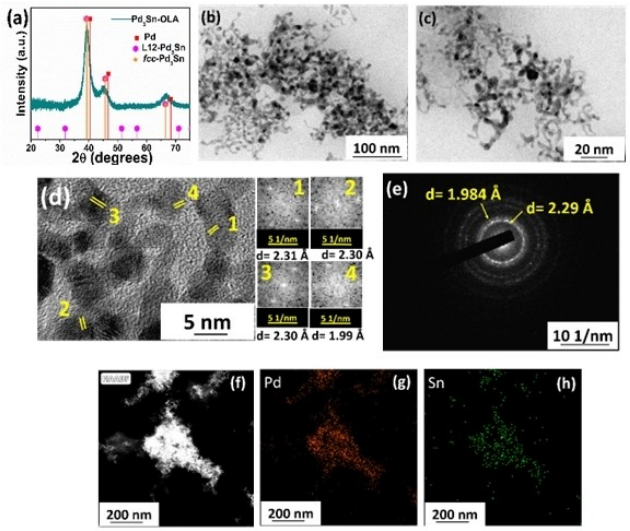

Figure 3. Pd_3Sn-OLA nanostructures (precipitate part): (a) PXRD pattern (ICDD- 01–072-2873, L12 phase and ICDD-03-066-0022, fcc); (b, c) BFTEM images; (d) HRTEM image and corresponding FFT patterns; (e) SAED pattern; (f-h) STEM-DF image and corresponding elemental maps of Pd and Sn, respectively.

For the supernatant part, well-separated spherical nanoparticles with average particle size of 4.1 ± 0.1 nm could be seen in most regions of the grid in the BFTEM images (Figures 4a, 4b). The size-distribution of spherical nanoparticles is shown in Figure 4c. The worm-like nanostructures were noted in a few regions, which could be attributed to the association of spherical nanoparticles as revealed by the HRTEM image (Figure 4d,4e).[46,59] SAED pattern (Figure 4f) did not show any feature which is due to the small size of particles. From the TEM data of supernatant and precipitates of Pd_3Sn nanoparticles, it could be anticipated that spherical nanoparticles are associated forming worm-like nanostructures, which further form network-like structures leading to precipitation. This could be attributed to the weak binding of OLA to the Pd-rich, Pd–Sn nanoparticles. Area mapping and the corresponding elemental composition of the spherical nanoparticles obtained from the supernatant of colloid confirmed the presence of Pd; however, the intensity of the elemental map corresponding to Sn was very low (Figure S2).

Furthermore, the presence of Pd and Sn in each particle, in this case, was confirmed by recording the EDS spectrum for individual particles in a few regions (Figure S3).

For the synthesis of Pd_2Sn, co-digestive ripening was carried out for 12 h using Pd-OLA-THF and Sn-OLA-THF colloids in a ratio of 3:1 using benzyl alcohol as a solvent (205 °C). The ordered arrangement of Pd and Sn atoms facilitated by the high temperature of the reaction lead to the formation of

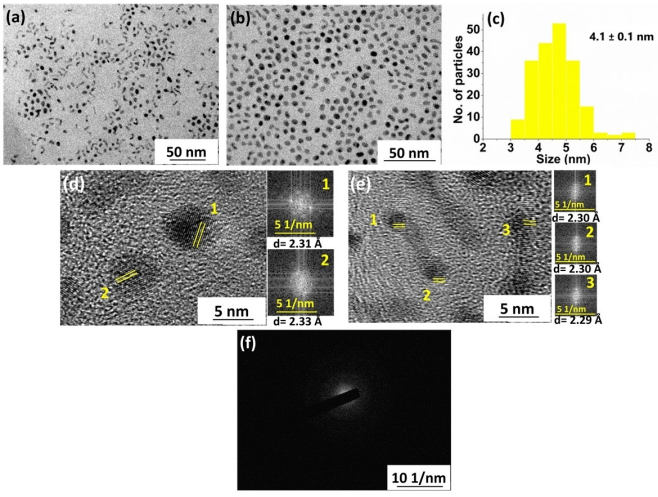

Figure 4. Pd_3Sn-OLA nanostructures (supernatant part): (a, b) BFTEM images; (c) histogram showing size distribution; (d, e) HRTEM images and corresponding FFT patterns; (e) SAED pattern.

Pd_2Sn.[60] However, in this case, the colloid was unstable towards the precipitation of particles. This could be attributed to the weak interaction of the capping agent with the nanocrystal surface which is a manifestation of the high temperature employed for the reaction causing uncontrolled growth leading to the aggregation and precipitation of particles. Additionally, the interaction of the chain of the capping ligand with the solvent employed for synthesis determines the dispersibility of nanocrystals. Since oleylamine binds with metal by donating the lone pair of nitrogen, the other end forms a hydrophobic surface on the nanocrystal. Benzyl alcohol, being polar, does not interact with the hydrophobic surface, resulting in precipitation of particles.[61] Black precipitates could be separated by centrifugation. The PXRD pattern (Figure 5a) could be assigned to the orthorhombic phase of intermetallic Pd_2Sn (ICDD-01-076-2812). BFTEM image (Figure 5b) revealed aggregated nanostructures with grape-like morphology. HRTEM image (Figure 5c) showed d-spacing values of 2.29 Å/2.30 Å, 1.947 Å, 1.434 Å and 1.168 Å corresponding to the (013), (320), (331) and (522) planes of Pd_2Sn. The SAED pattern (Figure 5d) corroborates with the HRTEM data. Elemental distribution was found to be homogeneous by STEM-EDS (Figure 5e–5 g). SEM-EDS gave the ratio of Pd and Sn in the Pd_2Sn intermetallic as 66:33 (Figure S4).

Role Of Temperature And The Stochiometric Ratio Of The Two Elements

Temperature at which the co-digestive ripening is carried out and the ratio of Pd:Sn play important roles in the phase-controlled synthesis of nanoparticles. For instance, when the ratio of Pd:Sn of 2:1 was employed for the synthesis of Pd_2Sn nanostructures, peaks due to Sn (excess) were observed in the PXRD patterns (Figure S5) along with partial alloying of Pd–Sn at 165 °C as well as at 205 °C. This indicates that all the Pd atoms have been utilized leading to partial alloying along with excess Sn in the reaction mixture. When the stoichiometric ratio was raised to 3:1, and the temperature was maintained at 205 °C, phase pure Pd_2Sn nanostructures were obtained (Figure 5a). At 165 °C, alloying of Pd–Sn with no excess of tin was observed, but the formation of Pd_2Sn intermetallic did not take place (PXRD pattern, Figure S6). This implies that optimized stochiometric ratio of metal elements and high temperature are obligatory for the formation of phase pure Pd_2Sn intermetallic nanostructures. For the synthesis of Pd_3Sn nanostructures, the ratio of Pd:Sn was further increased to 4:1, and alloy nanoparticles of Pd_3Sn were obtained at both the temperatures but with different morphology (Figures 3a, 3b, 4a, S7). It has even been established in the literature that the input ratio of precursor elements need not necessarily be the same as the output ratio.[25,62] In a report by Skrabalak and co-workers, Pd_3Sn_2, Pd_3Sn and Pd_2Sn phases were realized when the molar ratio of Pd:Sn precursors were taken as 1:1, 4:1, and 2:1, respectively. At a 3:1 molar ratio of Pd and Sn, Pd_2Sn nanoparticles were obtained with a larger average size. The effect of the stoichiometric ratio of metal elements and temperature on the phases in the case of co-digestive ripening have also been demonstrated earlier in the literature reports.[28–30]

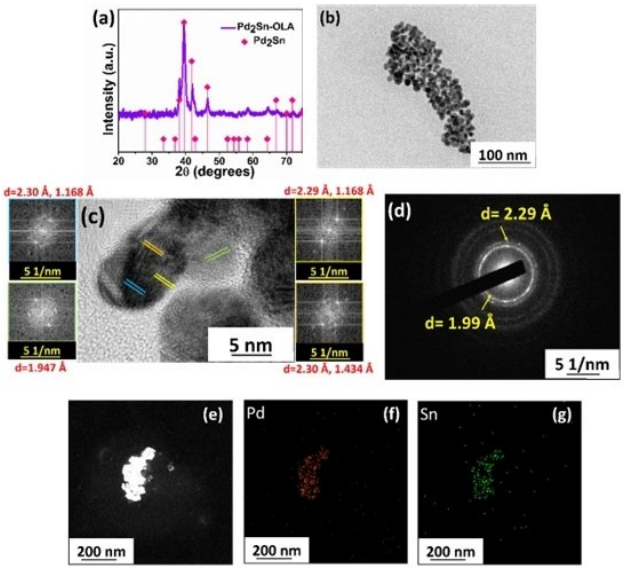

Figure 5. Pd_2Sn-OLA nanostructures: (a) PXRD pattern (ICDD-01-076-2812); (b) BFTEM image; (c) HRTEM image and corresponding FFT patterns, colors of borders of FFT patterns and their corresponding d-spacings in HRTEM image are kept same; (d) SAED pattern; (e–g) STEM-DF image and corresponding elemental maps of Pd and Sn, respectively.

Synthesis Of Pd_3Sn And Pd_2Sn: Role Of TOP On The Shape And Size Control

The use of a mixture of capping ligands to achieve the best control over nanoparticle size distribution and morphology has been well established in the literature, even though the general mechanism remains unclear.[47] One of the frequently used additional capping ligands with oleylamine (OLA) is trioctylphosphine (TOP). In our work, we attempted to use trioctylphosphine as a co-ligand which was employed in the synthetic procedure as an additional step once refluxing of OLA stabilized Pd and Sn colloids started. The synthesis was otherwise carried out in the same manner as described above. The colloid obtained was highly stable towards the precipitation of particles. The PXRD pattern (Figure S8) of the corresponding sample confirmed the formation of Pd_3Sn nanoparticles. BFTEM image (Figure 6a) revealed the presence of nanoparticles with well-defined shape and average size of 2.9 ± 0.5 nm (Size-distribution shown in Figure 6b). HRTEM image (Figure 6c) displayed fringes only at certain regions of the particles that could be assigned to the planes of Pd_3Sn. Due to the very small size of the particles, diffused rings could be observed in the SAED pattern (Figure 6d). Elemental mapping (Figures 6e-6 g) was carried out for a group of particles which confirmed a homogeneous distribution of Pd and Sn in the particles (particles were too small to map individually). Small and nearly monodisperse nanoparticles indicate the strong interaction between the nanoparticles and the capping ligands.[63]

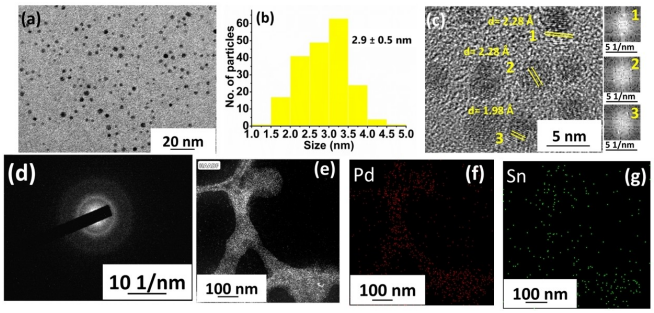

Figure 6. Pd_3Sn-OLA-TOP nanostructures: (a) BFTEM image ; (b) histogram showing the size-distribution of particles; (c) HRTEM image and corresponding FFT patterns; (d) SAED pattern; (e–g) STEM-DF image and corresponding elemental mapping of Pd and Sn, respectively.

In the case of Pd_2Sn, the addition of TOP led to the formation of well-separated particles in many regions along with the presence of aggregated structures (Figure 7a). The d-spacing values obtained for the interplanar distance in the fringes in the HRTEM image (Figure 7b) could be assigned to the (013) plane of Pd_2Sn. SAED pattern (Figure 7c) corresponding to the small-sized particles exhibited no rings or spots. Area mapping (Figures 7c–7i) was done for both aggregated nanostructures and individual nanoparticles.

Both Pd and Sn could be found in the same region in the elemental maps. The PXRD pattern corresponding to this sample has been deposited in the supplementary information (Figure S9). Trioctylphosphine is a high-boiling point surfactant with a long alkyl chain that imparts good steric hindrance leading to the good dispersion of nanoparticles. It is anticipated that OLA gets displaced by TOP partially or completely.[64] This was evidenced by ^{31}P NMR spectroscopy for one of the OLA-TOP capped Pd–Sn samples. A singlet in the $^{31}P\{^1H\}$ NMR spectrum at −32.2 ppm for the neat TOP was found to be shifted downfield to −19.5 ppm for the Pd_3Sn-OLA-TOP sample

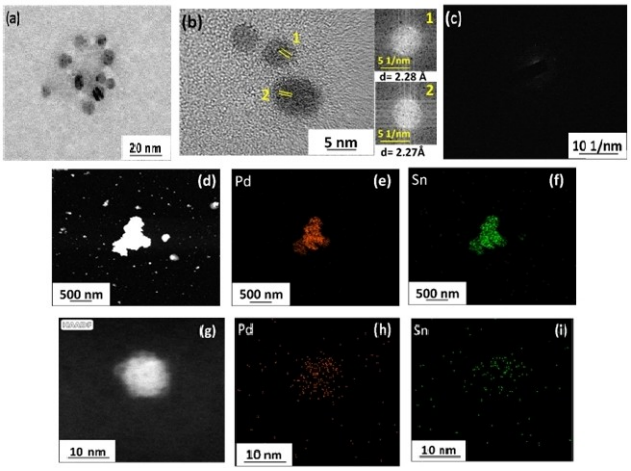

Figure 7. Pd_2Sn-OLA-TOP nanostructures: (a) BFTEM image; (b) HRTEM image and corresponding FFT patterns; (c) SAED pattern; (d–f and g–i) STEM-DF images and corresponding elemental maps of Pd and Sn, for aggregates and individual particle, respectively.

(Figure S10). Strong binding of ligands prevents growth of the particles, leading to their small size.

XPS Characterization

Figures 8 (8a–8 h) show the Pd and Sn survey scans of Pd_3Sn and Pd_2Sn nanoparticles. Binding energy values for each element have been provided in the supplementary information (Table S1) for all the samples. The Pd 3d profiles display two peaks corresponding to $3d_{5/2}$ and $3d_{3/2}$. The binding energies of Pd in the Pd–Sn samples were found to be shifted to higher binding energy values as compared to oleylamine capped Pd nanostructures (Figure S11), suggesting a change in the electronic structure of Pd in the Pd–Sn nanostructures.[25,51] The shift in the case of Pd_2Sn intermetallic was found to be more positive as compared to that in Pd_3Sn alloy nanostructures corroborating with the previously reported observations for intermetallic and alloy nanostructures.[51] In the case of Sn, peaks were deconvoluted into two pairs of doublets corresponding to the $3d_{5/2}$ and $3d_{3/2}$ states of Sn(0) (485.0–485.5/493.8–494.5 eV) and $Sn^{2+/4+}$(486.4–487.0/494.8–495.6 eV). The binding energy values for Sn(0) in Pd–Sn were also found to be shifted compared to the reported pristine Sn(0) (484.7 and 493.2 eV)[25,51] confirming a change in the electronic structure of Sn in the Pd–Sn nanostructures. The presence of $Sn^{2+/4+}$ peaks could be ascribed to the formation of SnO_x due to surface oxidation of Sn atoms or any unreacted Sn species present in the reaction mixture, which were, however, not detected by PXRD.

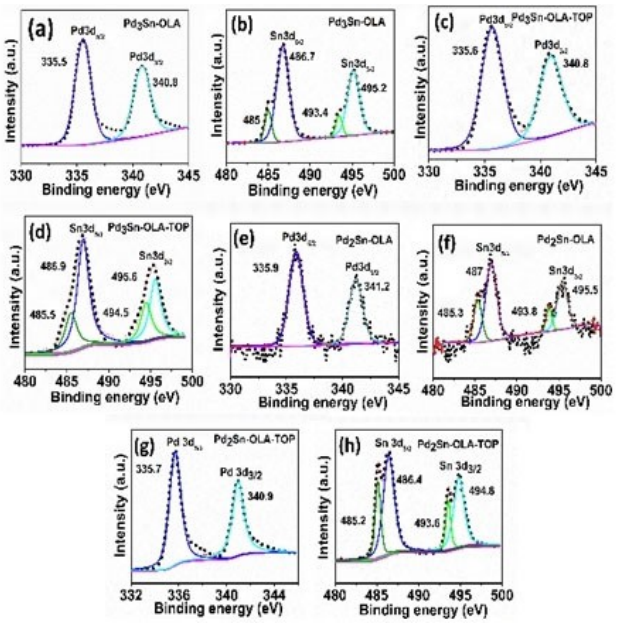

Figure 8. XPS survey scans of (a) Pd (b) Sn, corresponding to Pd_3Sn-OLA; (c) Pd (d) Sn, corresponding to Pd_3Sn-OLA-TOP; (e) Pd (f) Sn, corresponding to Pd_2Sn-OLA; (g) Pd (h) Sn, corresponding to Pd_2Sn-OLA-TOP nanostructures, respectively.

Discussion Of The Plausible Mechanism

Phase pure bimetallic nanostructures of Pd_2Sn and Pd_3Sn were obtained via co-digestive ripening of oleylamine-stabilized Pd and Sn colloids. Although the synthetic procedures of such systems have been well developed, solution-based synthesis, as illustrated above, is unprecedented. The methodology discussed herein has several advantages, which include: (i) large quantities of phase pure alloy and intermetallic nanostructures could be obtained and (ii) single phase (in major quantity) could be generated by optimizing the stoichiometric ratio between the metals and also the temperature, by this methodology. In the very first report on the synthesis of alloy particles by co-digestive ripening by Smetana et al., insights into the mechanistic details were provided.[65] The first step in co-digestive ripening brought out the importance of the capping agent or also known as the digestive ripening agent which acts as a labile metal carrier by removing and transplanting atoms from one particle onto another. Oleylamine is an excellent choice in this case as it does not bind too strongly or too weakly to the Pd and the Sn atoms. This step is a top-down process, followed by interparticle diffusion of Pd and Sn, leading to the nucleation of homogeneous bimetallic phases of the Pd–Sn system. Inter-diffusion of noble metals into Sn has been studied for several years.[66,67] It has been demonstrated that diffusion of noble metal into Sn takes place at a much faster rate via an interstitial mechanism; on the other hand, diffusion of Sn is a slow process which occurs via the substitutional mechanism. Diffusion of Pd into Sn in the case of films has been reported at room temperature.[68] It is to be noted that the presence of various defects on the surface of nanoparticles and at the interface between the two nanoparticles enhance the diffusion rates, thus promoting the alloying of metal nanoparticles.[69,70] In a recent report by Q. Zang et al., the formation of core-shell nanostructures via ripening mechanism using $Cd.CdCl_2$ as a model system, has been investigated by in-situ atomic resolution imaging with liquid cell transmission electron microscopy.[70] The work demonstrated that the mass transfer between the cores and shells of particles during the ripening procedure takes place through the crack defects. Based on the literature, the formation of voids or other forms of defects during the co-digestive ripening of two different elements, therefore, could be anticipated. Higher temperatures accelerate the process of diffusion further to the point of lattice rearrangement, thereby forming intermetallic particles.[65] Scheme 1 represents the process of co-digestive ripening.

Oxidation Of Benzyl Alcohol

The bimetallic nanostructures were evaluated for the catalytic oxidation of benzyl alcohol under base-free conditions. Pd_2Sn and Pd_3Sn nanoparticles obtained in the presence of an additional capping agent (TOP) by co-digestive ripening were highly stable towards precipitation of particles. Due to the difficulties involved in the isolation of TOP-stabilized Pd–Sn nanostructures, only oleylamine capped Pd_2Sn and Pd_3Sn nanoparticles were employed for the catalytic activity. The catalytic studies were undertaken to evaluate the difference in the catalytic behaviour of the random alloy and the intermetallic nanostructures of Pd–Sn system prepared by the co-digestive ripening method and its comparison with the activity of bare Pd nanoparticles.

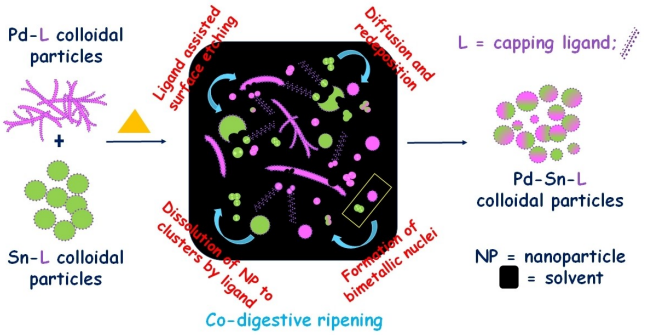

Scheme 1. Co-digestive ripening process to form bimetallic nanoparticles

The oxidation of benzyl alcohol (0.5 mL, 4.808 mmol) was performed using an O_2 balloon at 120 °C using Pd, Pd_2Sn, and Pd_3Sn catalysts in p-xylene (1.5 mL) as a solvent. Initially, the substrate-to-catalyst ratio was employed at 500/1 mol/mol. Table 1 summarizes the catalytic activity and selectivity of reaction conversions. Pd_2Sn and Pd_3Sn showed complete conversion in 6 h and 98% conversion was noted for Pd nanostructures (Figure 9a). The best selectivity results were obtained for the Pd_2Sn catalyst with a value of 92%, followed by Pd_3Sn (75%) and Pd (56%). The mixing of the second element with the parent metal with control over stoichiometry,

Table 1. Base-free oxidation of benzyl alcohol at 120 °C

Catalyst	% conversion (benzylalcohol)	% selectivity (benzaldehyde)	TON	TOF (h^{-1})
Pd	98	56	277	46
Pd_2Sn	>99	92	462	77
Pd_3Sn	>99	75	375	62

benzyl alcohol = 4.808 mmol, solvent = p-xylene, oxidant = oxygen balloon, time = 6 h, substrate-to-catalyst = 500:1. Conversion and selectivity were obtained from the GC measurements. Turn over number (TON) - = mol(benzaldehyde)/mol(catalyst); Turn over frequency (TOF) = TON/h.

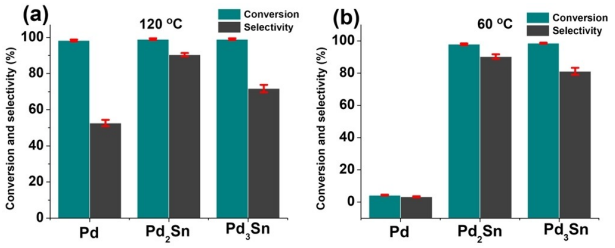

Figure 9. Percentage conversion of benzyl alcohol and selectivity of benzaldehyde using Pd, Pd_2Sn and Pd_3Sn catalysts at (a) 120 °C and (b) 60 °C, respectively. Error bars are calculated corresponding to the three batches of reaction(n = 3).

offers tunability which empowers the catalysts with improved activity and selectivity than those of the constituent elements.[6–12] This is attributed to the modification of the electronic structure and the active sites of the catalyst due to alloying.[71] The enhanced selectivity in the case of intermetallic nanostructures as compared to that in the case of random alloy could be ascribed to the isolation of catalytic sites previously demonstrated for many intermetallic nanostructures albeit for different reactions.[9] In addition, the specific and the ordered arrangement of atoms on the surface of intermetallic catalysts impose steric restrictions towards the adsorption of reactants which promote the controlled catalysis.[9] Negligible conversions were realized when Sn nanoparticles were used as a catalyst. These findings suggest that monometallic Pd is more efficient than Sn towards benzyl alcohol oxidation in this case; it is, therefore, reasonable to anticipate that oxidation mainly occurs on Pd sites in the Pd–Sn catalyst.

To evaluate the effect of substrate-to-catalyst ratio for the Pd–Sn nanostructures, catalytic performance at different substrate-to-catalyst ratios was studied, the data has been presented in Table S2. A negligible decrease in the catalytic activity was noted for both the catalysts when the substrate-to-catalyst ratio was increased to 1000/1 mol/mol. This outcome demonstrates that even at high substrate concentrations, the amount of catalyst may be far more than needed, to facilitate the reaction with full conversion. At the substrate-to-catalyst ratio of 5000/1 mol/mol, the catalytic activity dropped to 61% in the allotted time for Pd_2Sn catalyst and to 13% for Pd_3Sn. This suggests that the ideal substrate-to-catalyst ratio in this case for benzyl alcohol oxidation for both the catalysts lies between 1000/1 and 5000/1, where the catalysts can effectively promote the reaction.[72,73]

The difference in the stabilities and the intrinsic activity of the two catalysts under identical conditions could account for the fact that the drop in conversion was more pronounced for Pd_3Sn than Pd_2Sn at the substrate-to-catalyst ratio of 5000/1 mol/mol. The selectivity towards benzaldehyde decreased in the case of substrate-to-catalyst ratio of 1000/1 mol/mol and at the substrate-to-catalyst ratio of 5000/1 mol/mol, selectivity of >99% was noted towards benzaldehyde (Table ES2) for both the catalysts. This could be attributed to the diffusion limitations which were also evident in percentage conversion (Table ES2).[72,73] Even at a lower reaction temperature, i.e., 60 °C, almost complete conversion took place using Pd_2Sn and Pd_3Sn catalysts in 6 h (solvent = p-xylene, the ratio of substrate to catalyst as 500/1 mol/mol). Negligible reduction in the benzaldehyde yield was noted using the Pd_2Sn catalyst; using Pd_3Sn, 84% selectivity at a reaction temperature of 60 °C towards benzaldehyde was realized (Table 2, Figure 9b).

This could be due to the formation of other by-products i.e., benzyl benzoate due to over-oxidation at higher temperatures[74,75] in the case of Pd_3Sn as a catalyst. Pd catalyst was found to be inactive under these reaction conditions and showed negligible conversion. Base-free oxidation of benzyl alcohol (solvent = p-xylene, substrate to catalyst 500/1 mol/mol, 120 °C) was also performed in air, without using an oxygen balloon. High conversion of benzyl alcohol was obtained for the Pd–Sn catalysts, however, selectivity of benzaldehyde, specifically using the Pd_3Sn catalyst, got significantly reduced (Table S3).

Table 2. Base-free oxidation of benzyl alcohol at 60 °C

Catalyst	% conversion (benzylalcohol)	% selectivity (benzaldehyde)	TON	TOF (h^{-1})
Pd_2Sn	97	91	458	76
Pd_3Sn	>99	84	425	70

benzyl alcohol = 4.808 mmol, solvent = p-xylene, oxidant = oxygen balloon, time = 6 h, substrate-to-catalyst = 500:1 Conversion and selectivity were obtained from the GC measurements. Turn over number (TON) - = mol(benzaldehyde)/mol(catalyst); Turn over frequency (TOF) = TON/h.

To investigate the effect of solvent, oxidation of benzyl alcohol (substrate to catalyst 500/1 mol/mol, 120 °C, oxidant = oxygen balloon) was carried out using toluene in place of p-xylene. The decrease in conversion as well as selectivity towards benzaldehyde was noted for all the three catalysts i.e., Pd, Pd_2Sn and Pd_3Sn (Table S4).

Although, we were successful in demonstrating the doping of Sn into Pd via co-digestive ripening to synthesize cost-effective and an efficient catalyst for oxidation of benzyl alcohol with improved catalytic performance and selectivity as compared to monometallic Pd, the difference in phase dependent activity would require much more detailed investigation. Besides that, size and morphology difference also prevent a truly direct comparison of catalytic performance.

The most frequently reported bimetallic catalysts for benzyl alcohol oxidation are Pd–Au.[39,41,77–80] In Table 3, a few reports demonstrating Pd or Pd-based nanostructures used for the selective oxidation of benzyl alcohol under base-free conditions have been provided for a comparison. Sn has been regarded as one of the exceptional elements for doping with noble metals due to its oxyphilic property and ability of accelerating the activation of the surface sites for different reactions.[53,82] A report by Fang et al. demonstrated the effect of addition of Sn promoter on the catalytic performance of Pd/C for the base-free selective oxidation of vanillyl alcohol.[18] The conversion of alcohol increased from 69% to 100% upon incorporation of 0.1 wt.% of Sn in Pd/C and vanillin was produced in quantitative yield. It is worthwhile to note that, in our work, even though the Pd–Sn nanostructures used for the catalysis were highly aggregated (network-like structures in the case of Pd_3Sn and grape-like structures in the case of Pd_2Sn), yet significantly enhanced catalytic activity and selectivity were realized using both the catalysts. This evidences that mere doping of Sn in Pd via co-digestive ripening greatly enhances the catalytic performance of Pd nanostructures towards selective oxidation of benzyl alcohol under base-free conditions. These results suggest that in the case of Pd-based bimetallic systems, Sn could be a suitable and affordable replacement for expensive metals like Au to oxidize benzyl alcohol to benzaldehyde with improved selectivity under relatively mild conditions.

Table 3. Comparison of catalytic activities of the Pd-based catalysts for the base-free oxidation of benzyl alcohol.

Metal	Catalyst name	Catalyst amount, metal loading (mg, wt%)	Amount of substrate (mmol)	T (°C)	O_2 (bar)	Conv. (%)	Select. (%)	t (h)	TOF (h^{-1})*	Reference
Pd	Pd/COF-300-1114	10, 1.1	0.2	90	1	97	97	32	6**	[76]
Pd-Au	AuPd/S25	28.5, 2	9.6	100	4	99	>90	2.5	927**	[77]
Pd-Au	0.5%SnO_x@AP-ox	50, 0.73	100	110	8	81.7	73.2	2	13662***	[78]
Pd-Au	Au–Pd/TiO_2	400, 2	192	90	1	74.2	95.8	6	589***	[79]
Pd-Au	AuPd/MgAl-MMO	10, 1	9.6	140	1	93	93	4	3250***	[80]
Pd-Zn	Pd90Zn10/TiO_2	20, 1	18	120	1	55	81	1	5,000**	[81]
Pd-Sn	Pd_2Sn	3.18, –	4.808	60	balloon	97	91	6	76	this work
Pd-Sn	Pd_2Sn	3.18, –	4.808	120	balloon	100	92	6	77	this work
Pd-Sn	Pd_3Sn	4.20, –	4.808	60	balloon	100	84	6	70	this work
Pd-Sn	Pd_3Sn	4.20, –	4.808	120	balloon	100	75	6	62	this work

*Calculations were done by taking conversion into consideration (literature reports).
**Calculations for Turn Over Frequency (TOF) are provided in supporting information.
***Already reported in the corresponding publications.

Recyclability

Since the Pd–Sn nanostructures were already aggregated, the reusability of the catalysts was only evaluated at 60 °C. The Pd–Sn nanostructures showed somewhat poor cycle stability. A drop in the catalytic activity was noted after two cycles using Pd_2Sn as a catalyst, in the case of Pd_3Sn, the activity was slightly reduced after the first cycle itself (Figures 10a, 10b; Table S5). Due to a decrease in the catalytic performance of both the catalysts to a great extent after three cycles, reusability was not tested further. The selectivity of the catalysts was, however, maintained even after three cycles. The morphology and composition of the used catalysts were further examined by TEM and XRD. The PXRD pattern (Figure S12a) corresponding to Pd_2Sn nanostructures recorded after three cycles could be assigned to phase pure Pd_2Sn, no peaks corresponding to segregated Pd, Sn, or SnO_x were observed. However, the peaks were relatively broader, which reveals a change in the morphology of Pd_2Sn nanostructures. This was further confirmed by TEM (Figure S12b). For the Pd_3Sn catalyst, peaks corresponding to the tetragonal Sn could be assigned along with Pd_3Sn alloy in the PXRD pattern (Figure S13a) recorded after three cycles. This indicates that leaching of Sn in the case of Pd_3Sn (random alloy) takes place.[83] TEM data of the used Pd_3Sn catalyst has been deposited in the supplementary information (Figure S13b). The decrease in catalytic activity, therefore, could be attributed to the structural and morphological changes causing aggregation, sintering and/or reshaping of the catalyst under the reaction conditions used in this work.[84] Incorporation of a suitable support during co-digestive ripening or better shape/size control by varying the different reaction parameters could prevent aggregation, sintering and/or reshaping of the catalyst thus producing stable catalysts to be used for repeated cycles.

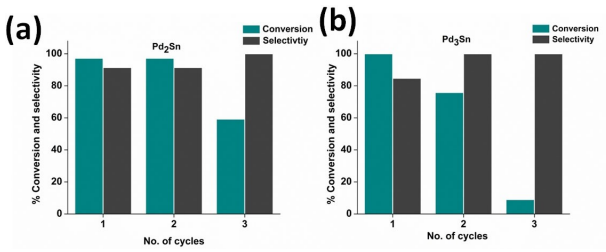

Figure 10. Percentage conversion of benzyl alcohol and selectivity to benzaldehyde for (a) Pd_2Sn, and (b) Pd_3Sn catalysts, respectively, at 60 °C for three cycles.

Conclusion

Facile synthesis of Pd_2Sn and Pd_3Sn nanostructures was achieved by employing a colloidal based synthetic route known as 'co-digestive ripening' with phase control using oleylamine as a capping agent. Pd_2Sn nanostructures were obtained in an ordered phase (orthorhombic structure), while Pd_3Sn nanostructures were identified as a disordered phase (fcc structure). The addition of a second capping agent (trioctylphosphine) resulted in the formation of few-nm-sized Pd–Sn bimetallic nanoparticles, which is anticipated to occur due to the displacement of oleylamine with trioctylphosphine during the synthesis. Co-digestive ripening method offers the supremacy of obtaining bimetallic nanostructures in gram scale quantity with high reproducibility. This simple and direct synthesis route could provide insights into the mechanistic aspects of alloy and intermetallic formation at the nanoscale, which is one of the most intriguing research areas. Moreover, co-digestive ripening could be further extended to explore a variety of other bimetallic structures with phase, shape, and size control. Pd–Sn nanostructures, when utilized for oxidation of benzyl alcohol, demonstrated excellent activity under base-free conditions, even at a low temperature of 60 °C and high substrate-to-catalyst ratio. This work signified that Sn would be a cost-effective substitute for precious metals like Au, Pt, and Ag in Pd-based bimetallic nanostructures to be utilized for the selective oxidation of benzyl alcohol.

Experimental section

Materials

Tungsten crucibles were purchased from R. D. Mathis Company, California. Palladium foil (99.99% metal basis) was procured from Arora Matthey Limited. Tin foil (99.998% metal basis), oleylamine (OLA, 70% technical grade), and tri-n-octylphosphine (TOP, 90% technical grade) were obtained from Sigma Aldrich. OLA was degassed prior to use. Tetrahydrofuran, mesitylene, and p-xylene (S. D. Fine Chemicals Limited, India) were dried over sodium-benzophenone and degassed by several freeze-pump-thaw cycles. Benzyl alcohol (analytical grade, S. D. Fine Chemicals Limited, India), absolute ethanol (HPLC grade, 99.9%), and chloroform (HPLC grade, 99.9%) were used as received. All glassware was thoroughly dried in a hot air oven and evacuated before use. All reactions were carried out under an Ar atmosphere using standard Schlenk techniques.

Measurements

PANalytical Empyrean X-ray diffractometer with Cu K_α (0.154 nm) radiation source (45 kV and 30 mA, a scan rate of 0.2° min^{-1}) was used for powder X-ray diffraction measurements. Morphological characterization of nanoparticles which includes bright-field transmission electron microscopy (BFTEM), high-resolution electron microscopy (HRTEM), selected area electron diffraction (SAED), energy dispersive-X-ray spectroscopy (EDS), was done using a JEOL JEM-2100F microscope operating at an accelerating voltage of 200 kV. In addition, scanning transmission electron microscopy-elemental mapping (STEM-EDS) images of the nanocrystals were collected using Thermofischer-Talos F200 S at the same operating voltage (200 kV). The TEM specimens were prepared by slow evaporation of diluted colloids, obtained by dispersion of precipitates in THF, deposited on Formvar coated copper grid, and further drying under a lamp. The XPS measurements were carried out using a Thermo K-alpha XPS spectrometer with Al K_α (1486.708 eV) radiation. Samples were prepared on a clean Si wafer by drop-casting the re-dispersed nanoparticles. SEM-EDS measurements were done using JEOL SEM-IT 300, samples for which were prepared on carbon tape. NMR spectra [^{1}H (400 MHz), ^{31}P{1H} (162 MHz)] were recorded using Avance Bruker 400 MHz NMR spectrometer at ambient temperature. CH_3NO_2 was used as an internal standard to calculate the yield based on ^{1}H NMR spectroscopy. GC-MS data were acquired using a GCMS-QP2010 SE SHIMADZU system. Yield based on the GC data was calculated using n-decane as an internal standard.

Preparation Of Pd/Sn-THF Nanoparticles By The Solvated Metal Atom Dispersion Method (SMAD)

THF was employed as a coordinating solvent to prepare colloids of Pd and Sn by the SMAD method. Bulk metal in the form of foil (120–150 mg) was placed in an alumina coated tungsten crucible connected to two water-cooled copper electrodes. The crucible was cured prior to the experiment to ensure the removal of moisture and other contaminants. The SMAD reactor was connected to a Schlenk tube containing dried and degassed solvent (THF) through a bridgehead. The entire reaction chamber was maintained at a pressure of $2–3\times10^{-3}$ mbar. At first, 20–25 mL of solvent was condensed on the walls of the reactor using a liquid nitrogen bath placed around the SMAD reactor. Once a uniform layer of solvent matrix was formed, the crucible containing the metal was resistively heated, leading to the vaporization of the metal. The process of vaporization and condensation of the metal atoms was apparent by the appearance of a black/red color in the case of Pd and Sn, respectively, on a pre-formed layer of solvent. The metal atoms and the solvent vapors were allowed to co-condense on the reactor walls for a period of 3 to 4 h, during which the color of the matrix intensified. After the complete evaporation of the metal, a final layer of 20–25 mL solvent was condensed on the matrix. This was followed by slow warm-up of the frozen matrix to room temperature by removing the dewar flask containing liquid nitrogen. The colloid obtained was stirred in the reactor under argon for 30 min and siphoned into a Schlenk tube. Pd-THF and Sn-THF colloids were black and brown, respectively. Pd-THF colloids were unstable (towards precipitation of particles) as the particles started precipitating soon after siphoning. Sn-THF colloids were relatively stable towards precipitation of particles. Both the colloids were stored in Schlenk tubes under Ar.

Room Temperature Digestive Ripening Of Pd/Sn-THF Nanoparticles

The Pd-THF and Sn-THF colloids were prepared in a similar manner to that described above, except that the capping agent, oleylamine was placed at the bottom of the SMAD reactor. The ratio of metal to oleylamine was kept at 1:10. Upon warming up of the matrix the Pd/Sn-THF nanocrystals/particles came into contact with the capping agent. The mixture was stirred vigorously at r.t. for 2–2.5 h during which the particles underwent digestive ripening.

Co-Digestive Ripening Of Pd And Sn Nanoparticles

Oleylamine-capped Pd-THF and Sn-THF colloids were subjected to co-digestive ripening to obtain heterostructures.

Pd_3Sn-OLA nanostructures

Prior to the experiment, a 100 mL round bottomed Schlenk flask equipped with a water-cooled condenser was evacuated and flushed with Ar repeatedly. At first, mesitylene (solvent used for Pd_3Sn synthesis, bp = 165 °C) was added to the Schlenk flask, followed by the dispersion of Pd-OLA-THF and Sn-OLA-THF colloids in a stoichiometric ratio of 4:1. THF was then removed from the reaction mixture under dynamic vacuum followed by sonication (10–15 min) of the mixture and stirring under bubbling Ar. The concentration of nanoparticles with respect to solvent was kept at 1 mg/mL. The colloidal dispersion was refluxed in a pre-heated oil bath by maintaining the temperature at 165 °C for 12 h. During the ripening process a gradual change in the color of the colloid from black to brown was observed. The nanoparticles were isolated by centrifugation and the particles were washed using ethanol and chloroform (v/v 10:1). Dispersion of the Pd/Sn in mesitylene was quite stable towards the precipitation of particles. The supernatant was brown even after a few cycles of centrifugation and washing. Therefore, characterization of both supernatant and precipitates was done.

Pd_3Sn-OLA-TOP nanostructures

The experiment was carried out in a similar manner as described above, with an additional step which includes the injection of TOP (ratio of OLA:TOP = 1:1) as soon as the reaction mixture started refluxing. In this case too, the color of the mixture turned from black to brown. The colloid obtained was stable towards precipitation of particles for months.

Pd_2Sn-OLA and Pd_2Sn-OLA-TOP nanostructures

These experiments were also carried out in a similar fashion as described above, except that benzyl alcohol ((bp = 205 °C) as a solvent for Pd_2Sn synthesis) was used in place of mesitylene. The stoichiometric ratio between Pd and Sn was kept at 3:1. The colloids were unstable towards precipitation of particles in this case.

Oxidation Of Benzyl Alcohol

The oxidation of benzyl alcohol was carried in a 25 mL round-bottom flask containing benzyl alcohol (0.5 mL, 4.808 mmol), p-xylene (1.5 mL) and Pd/Pd–Sn catalyst, using O_2 in a balloon. The ratio of catalyst:substrate was taken 1:500 (and 1:1000, 1:5000 to study the effect of the catalyst concentration on oxidation).The reaction mixture was maintained at the desired temperature (60/120 °C) under constant stirring for 6 h. After the reaction, the catalysts were separated from the reaction mixture by centrifugation to test recyclability.

Supporting Information

The following is the supplementary data related to this article: PXRD patterns, SEM data, TEM data, STEM-EDS spectra, ^{31}P NMR spectrum, and XPS data. Binding energy values corresponding to the Pd and Sn elements in Pd–Sn nanostructures are also provided. ^{1}H NMR spectra and GC chromatograms and data pertaining to the catalytic performance of Pd–Sn nanostructures have also been deposited.

Acknowledgements

The Indian Institute of Science, Bangalore is gratefully acknowledged for the financial support. We thank I.I.Sc. for funding the procurement of TEM and XRD. G.B. thanks I.I.Sc. for the fellowship.

Conflict of Interests

The authors declare no conflict of interest.

Data Availability Statement

The data that support the findings of this study are available in the supplementary material of this article.

Keywords: alloy · benzyl alcohol · co-digestive ripening · Intermetallic · oxidation

[1] R. Du, X. Jin, R. Hübner, X. Fan, Y. Hu, A. Eychmüller, *Adv. Energy Mater.* **2020**, *10*, e1901945.
[2] T. S. Rodrigues, A. G. M. da Silva, P. H. C. Camargo, *J. Mater. Chem. A* **2019**, *7*, 5857–5874.
[3] P. K. Jain, X. H. Ivan, H. El-Sayed, M. A. El-Sayed, *Acc. Chem. Res.* **2008**, *41*, 1578–1586.
[4] Y. Yamamoto, T. Miura, Y. Nakae, T. Teranishi, M. Miyake, H. Hori, *Physica B: Condens. Matter* **2003**, *329*, 1183–1184.
[5] Y. Shi, Z. Lyu, M. Zhao, R. Chen, Q. N. Nguyen, Y. Xia, *Chem. Rev.* **2021**, *121*, 649–735.
[6] K. D. Gilroy, A. Ruditskiy, H.-C. Peng, D. Qin, Y. Xia, *Chem. Rev.* **2016**, *116*, 10414–10472.
[7] J. T. L. Gamler, H. M. Ashberry, S. E. Skrabalak, K. M. Koczkur, *Adv. Mater.* **2018**, *30*, e1801563.
[8] H. Y. Kim, S. H. Joo, *J. Mater. Chem. A* **2020**, *8*, 8195–8217.
[9] S. Furukawa, T. Komatsu, *ACS Catal.* **2017**, *7*, 735–765.
[10] Y. Yang, M. Wei, *J. Mater. Chem. A* **2020**, *8*, 2207–2221.
[11] A. Dasgupta, R. M. Rioux, *Catal. Today* **2019**, *330*, 2–15.
[12] M. Friedrich, S. Villaseca, L. Szentmiklósi, D. Teschner, M. Armbrüster, *Mater.* **2013**, *6*, 2958–2977.
[13] Z. Luo, J. Lu, C. Flox, R. Nafria, A. Genç, J. Arbiol, J. Llorca, M. Ibáñez, J. R. Morante, A. Cabot, *J. Mater. Chem. A* **2016**, *4*, 16706–16713.
[14] R. R. Zamani, M. Ibáñez, M. Luysberg, N. García-Castelló, L. Houben, J. D. Prades, V. Grillo, R. E. Dunin-Borkowski, J. R. Morante, A. Cabot, J. Arbiol, *ACS Nano* **2014**, *8*, 2290–2301.
[15] M. Ibáñez, A. Cabot, *Science* **2013**, *340*, 935–936.
[16] L. X. Ding, A. L. Wang, Y. N. Ou, Q. Li, R. Guo, W. X. Zhao, Y. X. Tong, G. R. Li, *Sci. Rep.* **2013**, *3*, e1181.
[17] Z. Luo, M. Ibáñez, A. M. Antolín, A. Genç, A. Shavel, S. Contreras, F. Medina, J. Arbiol, A, Cabot, *Langmuir* **2015**, *31*, 3952–3957.
[18] W. Sun, S. Wu, Y. Lu, Y. Wang, Q. Cao, W. Fang, *ACS Catal.* **2020**, *10*, 7699–7709.
[19] M. Chen, Y. Yan, M. Gebre, C. Ordonez, F. Liu, L. Qi, A. Lamkins, D. Jing, K. Dolge, B. J. Hang, P. Heintz, D. P. Shoemaker, B. Wang, W. Huang, *Angew. Chem. Int. Ed.* **2021**, *60*,18309–18317.
[20] J. Zhao, X. Xu, X. Li, J. Wang, *Catal. Commun.* **2014**, *43*, 102–106.
[21] C. Breinlich, J. Haubrich, C. Becker, A. Valcárcel, F. Delbecq, K. Wandelt, *J. Catal.* **2007**, *251*, 123–130.
[22] E. A. Sales, M. de Jesus Mendes, F. Bozon-Verduraz, *J. Catal.* **2000**, *195*, 96–105.
[23] L. Song, J. Ahn, D.-H. Kim, H. Shin, I. D. Kim, *ACS Appl. Mater. Interfaces* **2022**, *14*, 28378–28388.
[24] C. Bhattacharya, N. Arora, B. R. Jagirdar, *Langmuir* **2019**, *35*, 6493–6505.
[25] S. L. A. Bueno, X. Zhan, J. Wolfe, K. Chatterjee, S. E. Skrabalak, *ACS Appl. Mater. Interfaces* **2021**, *13*, 51876–51885.
[26] Z. Cao, X. Liu, X. Meng, L. Cai, J. Chen, P. Guo, *Colloids Surf. A: Physicochem. Eng. Asp.* **2021**, *621*, e126577.
[27] R. Lanza, M. Bersani, L. Conte, A. Martucci, P. Canu, M. Guglielmi, G. Mattei, V. Bello, M. Centazzo, R. Rosei, *J. Phys. Chem. C* **2014**, *118*, 25392–25402.
[28] N. Arora, B. R. Jagirdar, *Phys. Chem. Chem. Phys.* **2014**, *16*, 11381–11389.
[29] N. Arora, B. R. Jagirdar, K. J. Klabunde, *J. Alloys Compd.* **2014**, *610*, 35–44.
[30] G. Bhatia, B. R. Jagirdar, *Dalton Trans.* **2022**, *51*, 12147–12160.
[31] S. Amsarajan, B. R. Jagirdar, *J. Alloys Compd.* **2020**, *816*, e152632.
[32] C. Bhattacharya, B. R. Jagirdar, *J. Phys. Chem. C* **2018**, *122*, 10559–10574.
[33] S. T. Lin, M. T. Fanklin, K. J. Klabunde, *Langmuir* **1986**, *2*, 259–260.
[34] A. Urumese, R. N. Jenjeti, S. Sampath, B. R. Jagirdar, *J. Colloid Interface Sci.* **2016**, *476*, 177–183.
[35] M. Hudicky, *Oxidations in organic chemistry*, ACS, Washington DC, **1990**, 321–360.
[36] B. L. Ryland, S. S. Stahl, *Angew. Chem. Int. Ed.* **2014**, *53*, 8824–8838.
[37] N. Mizuno, *Modern heterogeneous oxidation catalysis*, John Wiley and Sons, Weinheim, **2009**, 151–178.
[38] Y. M. A. Yamada, T. Arakawa, H. Hocke, Y. Uozumi, *Angew. Chem. Int. Ed.* **2007**,*119*, 718–720.
[39] S. Marx, A. Baiker, *J. Phys. Chem. C* **2009**, *113*, 6191–6201.
[40] S. E. Davis, M. S. Ide, R. J. Davis, *Green Chem.* **2013**, *15*, 17–45.
[41] Q. He, P. J. Miedziak, L. Kesavan, N. Dimitratos, M. Sankar, J. A. Lopez-Sanchez, M. M. Forde, J. K. Edwards, D. W. Knight, S. H. Taylor, C. J. Kiely, G. J. Hutchings, *Faraday Discuss.* **2013**, *162*, 365–378.
[42] a) K. J. Klabunde, H. F. Efner, T. Murdock, R. Ropple, *J. Am. Chem. Soc.* **1976**, *98*, 1021–1023; b) K. J. Klabunde, D. Ralston, R. Zoellner, H. Hattori, Y. Tanaka, *J. Catal.* **1978**, *55*, 213–227.
[43] S. P. Bhaskar, M. Vijayan, B. R. Jagirdar, *J. Phys. Chem. C* **2014**, *118*, 18214–18225.
[44] S. B. Kalidindi, B. R. Jagirdar, *Inorg. Chem.* **2009**, *48*, 4524–4529.
[45] U. Sanyal, R. Datta, B. R. Jagirdar, *RSC Adv.* **2012**, *2*, 259–263.
[46] K. Naoe, C. Petit, M. P. Pileni, *J. Phys. Chem. C* **2007**, *111*, 16249–16254.
[47] S. Mourdikoudis, L. M. Liz-Marzán, *Chem. Mater.* **2013**, *25*, 1465–1476.
[48] A. H. Tian, J. Y. Kim, J. Y. Shi, K. Kim, K. Lee, *J. Power Sources* **2007**, *167*, 302–308.

[49] C. R. Bealing, W. J. Baumgardner, J. J. Choi, T. Hanrath, R. G. Hennig, *ACS Nano* **2012**, *6*, 2118–2127.
[50] C. Dietrich, S. Chen, G. Uzunidis, M. Hähsler, Y. Träutlein, S. Behrens, *ChemistryOpen* **2021**, *10*, 296–304.
[51] M. Zhou, J. Liu, C. Ling, Y. Ge, B. Chen, C. Tan, Z. Fan, J. Huang, J. Chen, Z. Liu, Z. Huang, J. Ge, H. Cheng, Y. Chen, L. Dai, P. Yin, X. Zhang, Q. Yun, J. Wang, H. Zhang, *Adv. Mater.* **2022**, *34*, e2106115.
[52] S. K. Johnston, N. Cherkasov, E. Pérez-Barrado, A. Aho, D. Y. Murzin, A. O. Ibhadon, M. G. Francesconi, *Appl. Catal. A* **2017**, *544*, 40–45.
[53] Y. Yan, J. S. Du, K. D. Gilroy, D. Yang, Y. Xia, H. Zhang, *Adv. Mater.* **2017**, *29*, e1605997.
[54] W. Du, K. E. Mackenzie, D. F. Milano, N. A. Deskins, D. Su, Xi. Teng, *ACS Catal.* **2012**, *2*, 287–289.
[55] D. Chen, S. Pei, Z. He, H. Shao, J. Wang, K. Wang, Y. Wang, Y. Jin, *Catalysts* **2020**, *10*, e751.
[56] F. Li, Q. Shao, M. Hu, Y. Chen, X. Huang, *ACS Catal.* **2018**, *8*, 3418–3423.
[57] O. T. Woo, J. Rezek, M. Schlesinger, *Mater. Sci. Eng.* **1975**, *18*, 163–165.
[58] I. Jbir, J. Couble, S. K. -Zine, Z. Ksibi, F. Meunier, D. Bianchi, *ACS Catal.* **2016**, *6*, 2545–2558.
[59] B. I. Kharisov, O. V. Kharissova, M. J. -Yacaman, *Ind. Eng. Chem. Res.* **2010**, *49*, 8289–8309.
[60] X. Liu, X. Li, D. Wang, R. Yu, Y. Cui, Q. Peng, Y. Li, *Chem. Commun.* **2012**, *48*, 1683–1685.
[61] Y. Yin, A. P. Alivisatos, *Nature* **2005**, *437*, 664–670.
[62] S. Mondal, V. S. K. Choutipalli, B. K. Jena, V. Subramanian, C. R. Raj, *J. Phys. Chem. C* **2020**, *124*, 9631–9643.
[63] W. Bu, Z. Chen, F. Chen, J. Shi, *J. Phys. Chem. C* **2009**, *113*, 12176–12185.
[64] K. A. Newton, H. R. Sully, F. Bridges, S. A. Carter, S. M. Kauzlarich, *J. Phys. Chem. C* **2021**, *125*, 6401–6417.
[65] A. B. Smetana, K. J. Klabunde, C. M. Sorensen, A. A. Ponce, B. Mwale, *J. Phys. Chem. B* **2006**, *110*, 2155–2158.
[66] B. F. Dyson, *J. Appl. Phys.* **1966**, *37*, 2375–2377.
[67] R. R. Chromik, E. J. Cotts, *MRS Proc.* **1995**, *398*, 307–312.
[68] K.-N. Tu, R. Rosenberg, *Jpn. J. Appl. Phys.* **1974**, *13*, 633–636.
[69] T. Shibata, B. A. Bunker, Z. Zhang, D. Meisel, C. F. Vardeman, J. D. Gezelter, *J. Am. Chem. Soc.* **2002**, *124*,11989–11996.
[70] Q. Zhang, X. Peng, Y. Nie, Q. Zheng, J. Shangguan, C. Zhu, K. C. Bustillo, P. Ercius, L. Wang, D. T. Limmer, H. Zheng, *Nat. Commun.* **2022**, *13*, e2211.
[71] H. Chen, Q. Tang, Y. Chen, Y. Yan, C. Zhou, Z. Guo, X. Jia, Y. Yang, *Catal. Sci. Technol.* **2013**, *3*, 328–338.
[72] S. L. Scott, *ACS Catal.* **2018**, *8*, 8597–8599.
[73] M. Zhang, M. Wang, B. Xu, D. Ma, *Joule* **2019**, *3*, 2876–2883.
[74] D. I. Enache, J. K. Edwards, P. Landon, B. S. -Espriu, B. A. F. Carley, A. A. Herzing, M. Watanbe, C. J. Kiely, D. W. Knight, G. J. Hutchings, *Science* **2006**, *311*, 362–365.
[75] A. Jha, K. R. Patil, C. V. Rode, *ChemPlusChem* **2013**, *78*, 1384–1392.
[76] C. Xu, J. Lin, D. Yan, Z. Guo, D. J. Austin Jr, H. Zhan, A. Kent, Y. Yue, *ACS Appl. Nano Mater.* **2020**, *3*, 6416–6422.
[77] J. M. da Silva, R. C. Sousa, J. C. S. Costa, J. L. Magalhães, G. E. Luz Jr, C. V. R. de Moura, E. M. de Moura, *Catal. Lett.* **2022**, *152*, 585–599.
[78] P. Wu, Z. He, Y. Liu, L. Song, C. Wang, E. Muhumuza, P. Bai, L. Zhao, S. Mintova, Z. Yan, *ACS Appl. Mater. Interfaces* **2021**, *13*, 49780–49792.
[79] Y. Hong, X. Jing, J. Huang, D. Sun, D. T. O. Wubah, F. Yang, M. Du, Q. Li, *ACS Sustain. Chem. Engn.* **2014**, *2*,1752–1759.
[80] J. Feng, C. Ma, P. J. Miedziak, J. K. Edwards, G. L. Brett, D. Li, Y. Du, D. J. Morgan, G. J. Hutchings, *Dalton Trans.* **2013**, *42*, 14498–14508
[81] E. Nowicka, S. Althahban, T. D. Leah, G. Shaw, D. Morgan, C. J. Kiely, A. Roldan, G. J. Hutchings, *Sci. Technol. Adv. Mater.* **2019**, *20*, 367–378.
[82] Y. Li, Y. Wang, S. Li, M. Li, Y. Liu, X. Fang, X. Dai, X. Zhang, *J. Catal.* **2021**, *395*, 282–292.
[83] S. G. Wettstein, J. Q. Bond, D. M. Alonso, H. N. Pham, A. K. Datye, J. A. Dumesic, *Appl. Catal. B* **2012**, *117*, 321–329.
[84] L. Xu, H. W. Liang, Y. Yang, S. H. Yu, *Chem. Rev.* **2018**, *118*, 3209–3250.

Manuscript received: April 20, 2023
Revised manuscript received: May 22, 2023
Accepted manuscript online: May 29, 2023
Version of record online: ■■, ■■

RESEARCH ARTICLE

A facile route termed 'co-digestive ripening' was employed to prepare Pd–Sn alloy and intermetallic nanostructures with phase control. The presence of different capping agents greatly influenced their size and morphology. When utilized for oxidation of benzyl alcohol under base-free conditions, enhanced catalytic activity and selectivity towards benzaldehyde was achieved for the Pd–Sn nanostructures as compared to their monometallic counterparts.

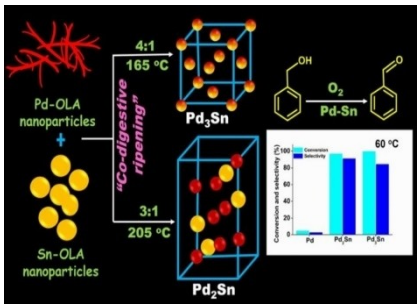

*G. Bhatia, B. R. Jagirdar**

1 – 13

Phase-Controlled Pd-Sn Nanostructures via Co-Digestive Ripening: Catalytic Performance for Base-Free Oxidation of Benzyl Alcohol